Ductile crack growth using cohesive GTN model

Mamadou Meïte, Noé Brice Nkoumbou Kaptchouang, Yann Monerie, Frederic Perales, Pierre Guy Vincent

Ductile crack growth using cohesive GTN model

Mamadou Méïté, Noé Brice Nkoumbou Kaptchouang, Yann Monerie, Frédéric Perales, Pierre-Guy Vincent

Abstract This chapter presents a three-dimensional simulation of ductile crack growth using a recent GTN cohesive approach. A cohesive-volumetric finite element approach is adopted. The behavior of the material is characterized by a hardening bulk constitutive law inside the finite elements together with a softening traction-separation law at the interfaces between elements. The traction-separation law recently proposed by [1] rests on the micromechanical Gurson-Tvergaard-Needleman model for ductile damage and fracture, and the reduced kinematics of a surface. It takes into account the effect of local I1 and J2 stress invariants via a dependence of the cohesive model to the surrounding bulk stress. The efficiency of this cohesive-GTN model is underlined through the 3D numerical simulation of a compact tension test. The results show a strong tunneling in the crack front shape. The crack propagates faster at the midsection than at the side-surface. Large gradients of local stress and strain through the specimen thickness during crack growth are observed. Es-

Mamadou Méïté
Institut de Radioprotection et de Sûreté Nucléaire, B.P. 3, 13115 Saint-Paul-lez-Durance Cedex, France, and MIST Laboratory, IRSN-CNRS-UM e-mail: mamadou.meite@irsn.fr

Noé Brice Nkoumbou Kaptchouang
Institut de Radioprotection et de Sûreté Nucléaire, B.P. 3, 13115 Saint-Paul-lez-Durance Cedex, France, and MIST Laboratory, IRSN-CNRS-UM e-mail: noe-brice.nkoumboukaptchouang@irsn.fr

Yann Monerie
LMGC, Univ. Montpellier, CNRS, Montpellier, France, and MIST Laboratory, IRSN-CNRS-UM e-mail: yann.monerie@umontpellier.fr, corresponding author

Frédéric Perales
Institut de Radioprotection et de Sûreté Nucléaire, B.P. 3, 13115 Saint-Paul-lez-Durance Cedex, France, and MIST Laboratory, IRSN-CNRS-UM e-mail: frederic.perales@irsn.fr

Pierre-Guy Vincent
Institut de Radioprotection et de Sûreté Nucléaire, B.P. 3, 13115 Saint-Paul-lez-Durance Cedex, France, and MIST Laboratory, IRSN-CNRS-UM e-mail: pierre-guy.vincent@irsn.fr

pecially, the stress triaxiality is higher at the midsection than at the side-surface, leading to more damage in the cohesive zone due to cavity growth.

Introduction

One way to simulate crack initiation and propagation involves finite elements with cohesive zones. In this approach, the micromechanisms of material degradation that take place in the fracture process zone ahead of the crack tip is modeled by a cohesive function termed as traction-separation law (TSL). It is expressed as a relationship $R = \mathscr{R}([u])$ between the stress vector R and the displacement jump $[u]$ across the two surfaces of the crack. The peak value of such a cohesive function defines the cohesive strength, R_0. The area under this curve refers to the separation energy, Γ_0, giving the work spent in the cohesive zone for the creation of a unit crack area. Although several authors [2, 3, 4, 5] have successively simulated several crack growth experiments with one set of cohesive parameters (R_0, Γ_0), it is now admitted that in the course of ductile fracture, these parameters are not material constants and therefore are not directly transferable from one experiment to another. In other works such as those of [6], different cohesive parameters depending on the position through the thickness of the specimen have been introduced in order to simulate crack growth experiments on steels with good accuracy. Moreover, the values of the cohesive parameters for a single material also depend on the shape of the TSL used in the simulations [7, 8]. One drawback of phenomenological cohesive functions is that they don't explicitely take into account the physics of micromechanical phenomenon leading to fracture such as the void nucleation, growth and coalescence in ductile failure of metals. Furthermore, cohesive zone model capabilities are also limited by their surface reduced kinematics, which only contain relevant quantities such as the crack normal opening and the crack sliding displacement, but nothing to describe the effect of crack plane stretching due to in-plane strain as in a volumetric 3D element [9]. This limitation makes it difficult to use a single set of cohesive parameters to model crack growth under different constraint conditions. Contrastingly, the framework of continuum micromechanics, with a physical modeling of the kinematics of voids nucleation, growth and coalescence inside a matrix material have led to a set of poroplasticity models that can properly describe damage process in ductile metals under different constraints conditions. Within this approach, the Gurson-Tvergaard-Needleman (GTN) model [10, 11, 12, 13] is surely the most widespread model to characterize ductile fracture. A physically based TSL that captures the mechanism of the ductile failure process of metals can be derived from a micromechanical modeling of a voided unit cell. This idea has been introduced by [14] who computed a TSL as a response of a GTN unit cell under uniaxial straining conditions. A step to improve the cohesive zone models for a wider range of local constraints has been undertaken by introducing a dependency of the shape of the traction separation law and the magnitudes of cohesive parameters to some variables characterizing the local stress and strain states such as the accumulated plastic strain

$\varepsilon^{\mathrm{p}}_{\mathrm{eq}}$ [15, 16], the stress triaxiality η_Σ [17, 18, 19, 20, 21], the equivalent strain rate $\dot{\varepsilon}_{\mathrm{eq}}$ [22, 23]. In these works, the cohesive strength R_0 and the cohesive energy Γ_0 are updated during the simulation according to the local stress and strain states through some specific functions ($R_0 = R_0(\varepsilon^{\mathrm{p}}_{\mathrm{eq}}, \dot{\varepsilon}_{\mathrm{eq}}, \eta_\Sigma, ...)$, $\Gamma_0 = \Gamma_0(\varepsilon^{\mathrm{p}}_{\mathrm{eq}}, \dot{\varepsilon}_{\mathrm{eq}}, \eta_\Sigma, ...)$) where the variables $(\varepsilon^{\mathrm{p}}_{\mathrm{eq}}, \dot{\varepsilon}_{\mathrm{eq}}, \eta_\Sigma)$ are computed in the nearest continuum element to the cohesive zone. The dependency of the cohesive parameters to stress triaxiality and strain rate was obtained through a range of unit cell simulations under different biaxial loadings with a GTN model in [17, 18, 19, 20] and a rate-dependent GTN model in [22, 23]. Some authors also characterize the cohesive parameters for simulation of the tearing of large ductile plate by using a combination of GTN simulations and experiments. The peak stress and dissipated energy are identified throughout a detailed analysis of the process of necking localization and shear failure performed with GTN-like models [24, 25, 26, 27]. Another straightforward approach to develop physically based TSL consists in modeling the cohesive zone as a virtual thin layer representing a discontinuity band in the material with the corresponding regularized discontinuity kinematics [28, 29, 30]. The jumps of displacements fields across the discontinuity band naturally induce a projection of the stress-strain constitutive model into a traction stress-displacement jumps law as discussed in [31]. This formalism enables the use of bulk constitutive relations embedding more details on the damage micromechanisms and crack initiation than a pure phenomenological TSL. The cohesive response is given by the traction stress and the displacement jump across the band. It can be used with a conventional zero thickness cohesive element, and in this case, the band thickness introduced to derive the cohesive model remains a parameter. Nonetheless, the surface (or thin layer) kinematics does not give rise to in-plane strains. As a consequence, the capability of cohesive band models to properly handle high triaxiality effects remains limited. One way to overcome this limitation is discussed in [9], where the cohesive band strain tensor is enhanced with in-plane components, which are evaluated as the average of the in-plane strains from the nearest volumetric elements on each side of the cohesive zone.

Following these ideas, [1] recently derived a TSL from the original GTN model and applied it to simulate crack growth in a compact tension specimen made with a standard ferritic steel (2D plane strain computations). The TSL results from a projection of the GTN porous plasticity model into a finite thickness discontinuity band kinematics. A single variable has been added to enhance the kinematics and to take into account the high triaxiality effects. Here, a 3D finite element computation is presented to investigate the capability of this new TSL to simulate ductile crack growth. This chapter is organized as follows. First, the equations of the GTN traction-separation law of [1] are recalled. Second, an analysis of a 3D finite element simulation of crack growth in a steel compact tension specimen is performed. Particular attention is paid to the crack front shape and to the heterogeneity of the stress and strain fields along the thickness of the specimen. In particular, the local traction-separation evolution is not a priori given. Its spatial evolution near the crack tip when going from the specimen midsection to the side surface is investigated.

Cohesive zone model for ductile failure

A GTN-like cohesive zone model has been developed in [1] by a projection of the so-called volumetric GTN damage model onto a cohesive kinematics. The TSL reproduces the behavior of a single bulk element made of a GTN material. This cohesive model is briefly described below.

Cohesive interface model

The cohesive zone is seen as a thin layer interface inside a bulk material, and the strain tensor is approximated by a function of the displacement jump $[u]$ across the interface with the help of a scaling rule [32, 28, 29]

$$\varepsilon \approx \frac{[u]\otimes_s n}{h} = \begin{bmatrix} \varepsilon_{\mathsf{nn}} & \varepsilon_{\mathsf{nt}} & \varepsilon_{\mathsf{ns}} \\ \varepsilon_{\mathsf{nt}} & 0 & 0 \\ \varepsilon_{\mathsf{ns}} & 0 & 0 \end{bmatrix} \quad \text{with} \quad \varepsilon_{\mathsf{nn}} = \frac{[u_{\mathsf{n}}]}{h}, \quad \varepsilon_{\mathsf{nt}} = \frac{[u_{\mathsf{t}}]}{2h}, \quad \varepsilon_{\mathsf{ns}} = \frac{[u_{\mathsf{s}}]}{2h} \tag{1}$$

where (n, t, s) is the local basis, n being a unit normal vector to the interface and t, s the two unit vectors defining the tangent plane. The h parameter is a length scale of the cohesive model and $(u\otimes_s v)_{ij} = (u_i v_j + u_j v_i)/2$. The kinematics (1) is extended by introducing an additional in-plane parameter p in order to enhance the range of strain triaxiality affordable by the cohesive model

$$\varepsilon = \begin{bmatrix} \varepsilon_{\mathsf{nn}} & \varepsilon_{\mathsf{nt}} & \varepsilon_{\mathsf{ns}} \\ \varepsilon_{\mathsf{nt}} & p & 0 \\ \varepsilon_{\mathsf{ns}} & 0 & p \end{bmatrix} \tag{2}$$

GTN model

The GTN yield surface writes [10, 11, 12, 13]

$$\frac{\Sigma_{\mathsf{eq}}^2}{\sigma_y^2} + 2q_1 f^* \cosh\left(\frac{3}{2} q_2 \frac{\Sigma_{\mathsf{m}}}{\sigma_y}\right) - 1 - q_3 f^{*2} = 0 \tag{3}$$

where Σ is the stress tensor, $\Sigma_{\mathsf{m}} = (1/3)\,\mathrm{tr}\,\Sigma$ is the hydrostatic stress, $\Sigma_{\mathsf{eq}} = \sqrt{(3/2)\Sigma^{\mathsf{d}} : \Sigma^{\mathsf{d}}}$ is the on Mises equivalent stress, $\Sigma^{\mathsf{d}} = \Sigma - \Sigma_{\mathsf{m}}\, i$ is the deviatoric part of Σ, and i is the second-order identity tensor. Coefficients $(q_1, q_2, q_3 = q_1^2)$ are constants. The flow strength of the homogeneous and incompressible plastic matrix surrounding the voids is denoted by σ_y. The porosity is denoted by f and an effective porosity f^* related to void coalescence is introduced

$$f^* = \begin{cases} f & \text{for } 0 \le f \le f_c \\ f_c + \dfrac{f_u^* - f_c}{f_f - f_c}(f - f_c) & \text{for } f_c < f \end{cases} \tag{4}$$

where f_c is the porosity at onset of void coalescence, and f_f is the fracture porosity, $f^*(f_f) = f_u^* = 1/q_1$. Isotropic hardening is introduced by the expression of $\sigma_y(\bar{\varepsilon})$, where the scalar variable $\bar{\varepsilon}$ is interpreted as an average plastic strain of the matrix material surrounding the voids. The evolution of $\bar{\varepsilon}$ is governed by an equivalent plastic work expression

$$\Sigma : \dot{\varepsilon} = (1-f)\sigma_y \dot{\bar{\varepsilon}} \tag{5}$$

The evolution of the porosity is governed by a void growth rate and a strain controlled void nucleation rate [33]

$$\dot{f} = (1-f)\,\mathrm{tr}\,\dot{\varepsilon} + A\dot{\bar{\varepsilon}} \quad \text{with} \quad A(\bar{\varepsilon}) = \frac{f_N}{s_N\sqrt{2\pi}} \exp\left(-\frac{1}{2}\left(\frac{\bar{\varepsilon} - \varepsilon_N}{s_N}\right)^2\right) \tag{6}$$

where f_N is the volume fraction of void nucleating particles, ε_N is an average nucleation strain parameter and s_N is a standard deviation.

Cohesive GTN traction-separation law

The time integration of the model derived in [1] is briefly summarized below. Let us denote ε, f and $\bar{\varepsilon}$ the cohesive strain, porosity and average plastic strain at time t. At the previous time step, their values are denoted by $\varepsilon^{(t-\delta t)}$, $f^{(t-\delta t)}$ and $\bar{\varepsilon}^{(t-\delta t)}$. The increment between two time steps of the cohesive strain $\delta\varepsilon$ writes

$$\delta\varepsilon = \begin{bmatrix} \delta\varepsilon_{\mathsf{nn}} & \delta\varepsilon_{\mathsf{nt}} & \delta\varepsilon_{\mathsf{ns}} \\ \delta\varepsilon_{\mathsf{nt}} & \delta p & 0 \\ \delta\varepsilon_{\mathsf{ns}} & 0 & \delta p \end{bmatrix} \tag{7}$$

Giving quantities at time t, and average strain at time $t - \delta t$, the porosity and the average strain are updated

$$f = f^{(t-\delta t)} + (1 - f^{(t-\delta t)})\,(\delta\varepsilon_{\mathsf{nn}} + 2\,\delta p) + A(\bar{\varepsilon}^{(t-\delta t)})\,\delta\bar{\varepsilon} \tag{8}$$

$$\bar{\varepsilon} = \bar{\varepsilon}^{(t-\delta t)} + \delta\bar{\varepsilon} \tag{9}$$

with

$$\delta\bar{\varepsilon} = \frac{T_{\mathsf{nn}}\,\delta\varepsilon_{\mathsf{nn}} + 2\,T_{\mathsf{nt}}\,\delta\varepsilon_{\mathsf{nt}} + 2\,T_{\mathsf{ns}}\,\delta\varepsilon_{\mathsf{ns}} + T_{\mathsf{tt}}\,\delta p + T_{\mathsf{ss}}\,\delta p}{1 - f^{(t-\delta t)}} \tag{10}$$

and

$$\begin{cases} T_{\mathsf{nn}} = \dfrac{1}{q_2} H(\chi^{(t-\delta t)}) + \dfrac{4}{9} D(\chi^{(t-\delta t)}) \dfrac{\delta\varepsilon_{\mathsf{nn}} - \delta p}{(\delta\varepsilon)_{\mathsf{eq}}} \\ T_{\mathsf{nt}} = \dfrac{2}{3} D(\chi^{(t-\delta t)}) \dfrac{\delta\varepsilon_{\mathsf{nt}}}{(\delta\varepsilon)_{\mathsf{eq}}} \\ T_{\mathsf{ns}} = \dfrac{2}{3} D(\chi^{(t-\delta t)}) \dfrac{\delta\varepsilon_{\mathsf{ns}}}{(\delta\varepsilon)_{\mathsf{eq}}} \\ T_{\mathsf{tt}} = T_{\mathsf{ss}} = \dfrac{1}{q_2} H(\chi^{(t-\delta t)}) - \dfrac{2}{9} D(\chi^{(t-\delta t)}) \dfrac{\delta\varepsilon_{\mathsf{nn}} - \delta p}{(\delta\varepsilon)_{\mathsf{eq}}} \\ \eta_{\dot{\varepsilon}} = \dfrac{(\delta\varepsilon)_{\mathsf{m}}}{(\delta\varepsilon)_{\mathsf{eq}}} \end{cases} \tag{11}$$

where $\chi^{(t-\delta t)}$ stands for $\{\eta_{\dot{\varepsilon}}, q_1 f^*(f^{(t-\delta t)})\}$ and H and D are two general functions

$$H(\eta_{\dot{\varepsilon}}, f) = \frac{2}{3}\left(\operatorname{arcsinh}\left(\frac{2\eta_{\dot{\varepsilon}}}{f}\right) - \operatorname{arcsinh}(2\eta_{\dot{\varepsilon}})\right) \tag{12}$$

$$D(\eta_{\dot{\varepsilon}}, f) = \sqrt{(2\eta_{\dot{\varepsilon}})^2 + 1} - \sqrt{(2\eta_{\dot{\varepsilon}})^2 + f^2} \tag{13}$$

Then, the components of the cohesive stress $R = \Sigma \cdot n$ are straightforwardly evaluated at time t

$$\begin{cases} R_{\mathsf{n}} = \sigma_y(\bar{\varepsilon}) \left(\dfrac{1}{q_2} H(\chi) + \dfrac{4}{9} D(\chi) \dfrac{\delta\varepsilon_{\mathsf{nn}} - \delta p}{(\delta\varepsilon)_{\mathsf{eq}}}\right) \\ R_{\mathsf{t}} = \sigma_y(\bar{\varepsilon}) \dfrac{2}{3} D(\chi) \dfrac{\delta\varepsilon_{\mathsf{nt}}}{(\delta\varepsilon)_{\mathsf{eq}}} \\ R_{\mathsf{s}} = \sigma_y(\bar{\varepsilon}) \dfrac{2}{3} D(\chi) \dfrac{\delta\varepsilon_{\mathsf{ns}}}{(\delta\varepsilon)_{\mathsf{eq}}} \end{cases} \tag{14}$$

where χ stands for $\{\eta_{\dot{\varepsilon}}, q_1 f^*(f)\}$.

Estimate of the in-plane strain

The in-plane strain p is estimated by considering information coming from a volumetric element adjacent to the cohesive zone. A strain rate triaxiality $\eta_{\dot{\varepsilon}}^{\mathsf{vol}}$ is computed using both the stress state Σ^{vol} in a volumetric element adjacent to the cohesive zone and the normality rule of the GTN model

$$\eta_{\dot{\varepsilon}}^{\mathsf{vol}} = \frac{q_1 q_2 f^* \sinh\left(\dfrac{3}{2} q_2 \dfrac{\Sigma_{\mathsf{m}}^{\mathsf{vol}}}{\sigma_y}\right)}{2\dfrac{\Sigma_{\mathsf{eq}}^{\mathsf{vol}}}{\sigma_y}} \tag{15}$$

The in-plane strain increment δp is estimated such that the strain rate triaxiality inside the cohesive zone is equal to $\eta_{\dot{\varepsilon}}^{\mathsf{vol}}$. As outlined in [1], it was observed that

the resulting triaxiality $\eta_{\tilde{\varepsilon}}^{\mathsf{vol}}$ decreases when increasing damage in the cohesive zone during a C(T) test simulation. This can lead to an artificially delay of crack growth because the standard GTN model does not predict any damage at low stress triaxiality. Therefore, [1] propose to transfer the volumetric stress Σ^{vol} to the cohesive zone up to the onset of coalescence (when f reaches f_c). For the post-coalescence stage, Σ^{vol} is kept constant.

Unloading rule and initial stiffness

An unloading rule and an initial finite stiffness are then added to the TSL by modifying the cohesive stress as below [1]

$$R^{(\mathsf{int})} = \begin{cases} R_{\mathsf{n}} \dfrac{[u_{\mathsf{n}}]}{[u_{\mathsf{n}}]_{\mathsf{max}}} \left(1 - \exp\left(-\alpha_{\mathsf{n}} \dfrac{[u_{\mathsf{n}}]_{\mathsf{max}}}{h}\right)\right) \\ R_{\mathsf{t}} \dfrac{[u_{\mathsf{t}}]}{[u_{\mathsf{t}}]_{\mathsf{max}}} \left(1 - \exp\left(-\alpha_{\mathsf{t}} \dfrac{[u_{\mathsf{t}}]_{\mathsf{max}}}{h}\right)\right) \\ R_{\mathsf{s}} \dfrac{[u_{\mathsf{s}}]}{[u_{\mathsf{s}}]_{\mathsf{max}}} \left(1 - \exp\left(-\alpha_{\mathsf{s}} \dfrac{[u_{\mathsf{s}}]_{\mathsf{max}}}{h}\right)\right) \end{cases} \tag{16}$$

where $[u_{\mathsf{n}}]_{\mathsf{max}}, [u_{\mathsf{t}}]_{\mathsf{max}}, [u_{\mathsf{s}}]_{\mathsf{max}}$ are the maximum values of separation in each direction occurred so far during the loading process. The terms $[u_i]/[u_i]_{\mathsf{max}}$ with $i = \{n,t,s\}$ in (16) describe an elastic linear unloading up to the origin. The exponential part allows to introduce an initial stiffness to the TSL when $[u]$ vanishes. The initial slope in various directions is calibrated by setting the parameters α_{n}, α_{t}, and α_{s} accordingly. The unloading behavior is completed by assuming the irreversibility of damage and hardening during loading process. From a practical point of view, two additional tests are performed in the integration scheme

$$\text{if} \quad f < f^{(t-\delta t)} \quad \text{then} \quad f = f^{(t-\delta t)} \tag{17}$$

and

$$\text{if} \quad \bar{\varepsilon} < \bar{\varepsilon}^{(t-\delta t)} \quad \text{then} \quad \bar{\varepsilon} = \bar{\varepsilon}^{(t-\delta t)} \tag{18}$$

Implementation into XPER computer code

The GTN cohesive zone model has been implemented in the XPER computer code dedicated to the simulation of fracture dynamics of heterogeneous materials [34, 35]. Each mesh element or group of mesh elements is treated as an independent body. Frictional cohesive zone models are introduced at interface between bodies by a modification of Signorini-Coulomb conditions [36, 37]. The bulk behavior inside each element is governed by a hardening behavior without any damage. The cohesive model has been implemented under the assumption of proportional loading and

the cohesive stress given by (14) is estimated using the total cohesive strain ε instead of the strain increment tensor $\delta\varepsilon$. Under this assumption, the strain rate triaxiality in the cohesive zone is equal to the strain triaxiality defined in (15). The transfer of information from the volume element to the cohesive zone, which is a key point of the model, is schematically illustrated in Fig. 1. The general equations used for the numerical implementation of the cohesive model are summarized in Appendix C of [1] and the reader is referred to this for an exhaustive and detailed description.

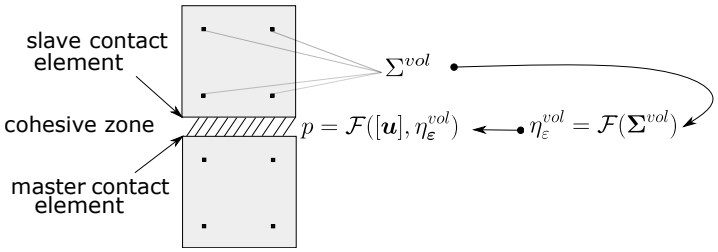

Fig. 1 The average stress in the slave element adjacent to the cohesive zone is used to evaluate an imposed strain triaxiality η_{ε}^{vol} in the cohesive zone. The in-plane strain p in the cohesive zone is a function of η_{ε}^{vol} and $[u]$.

Application: 3D numerical simulation of a compact tension fracture specimen

Modeling

A finite element analysis is performed on a deeply cracked compact tension C(T) fracture specimen with smooth side-surfaces. Remind that the primary motivation to use deeply cracked specimens is to guarantee conditions leading to high crack-tip constraint (i.e., high triaxiality of stress) with limited-scale plasticity [38]. Moreover, this type of specimen displays the highest triaxiality compared to any type of standard fracture specimen [2, 39, 6, 38, 40, 41, 42]. Here, a_0 denotes the initial crack depth and is set to 19.92 *mm*, while $W = 40\,mm$ is the specimen width (ratio $a_0/W \approx 0.5$). The specimen thickness is set to $B = 20\,mm$. The details of the specimen dimensions and the finite element mesh are displayed in Fig. 2. The axis of the global coordinate system (x, y, z) are along the crack extension direction, the loading direction, and the thickness direction, respectively. The plane $z = 0$ defines the midsection of the specimen, and $z = 10\,mm$ defines the side-surface (see Fig. 2). Symmetry conditions enable analyses using a quarter of C(T)-specimen. But since it is not possible to apply symmetry conditions on the cohesive elements in the crack plane in XPER code, one-half of the specimen is modeled with appropriate constraints ($U_z = 0$) at the midsection ($z = 0$). The mesh is refined over a surface 10 x

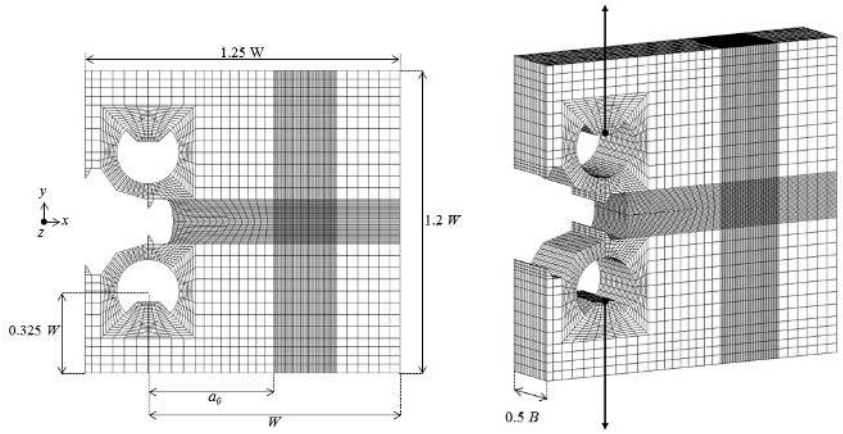

Fig. 2 C(T) specimen: Details of the geometry and half-symmetric three-dimensional finite element mesh. Mesh size in the crack propagation region is 0.2 x 0.2 x 0.5 mm^3 in (x, y, z)-axis, respectively.

7 x 10 mm^3 in front of the crack tip. The mesh size for the elements in this central zone is 0.2 x 0.2 x 0.5 mm^3 along the (x, y, z) respectively, while a coarser mesh is used outside this zone. The half-symmetric, 3D model for this specimen has a total number of 82803 nodes and 74560 hexahedra solid elements with eight-nodes. Since the crack path is known, cohesive zones are only put on the crack plane in front of the crack tip, assuming pure mode I crack propagation. Four contact nodes per cohesive zone are introduced. The material surrounding the cohesive zones is an isotropic elastic-plastic solid with incremental J2 plasticity constitutive model. The Young modulus and Poisson's ratio are respectively denoted by E and ν. The GTN cohesive model described in the previous section is used for the cohesive zones. The hardening (for both solid elements and cohesive zones) is described by

$$\sigma_y(\bar{\varepsilon}) = \sigma_0(1 + K\bar{\varepsilon})^{1/n} \tag{19}$$

where σ_0, K and n are three coefficients. The material parameters are reported in Table 1 for a specific ferritic steel (15NiCuMoNb5, German designation WB36). The initial porosity is denoted by f_0. Computation is performed under the small strain assumption. The length scale parameter controlling the localization is set to $h = 0.4$ mm which is in the order of magnitude for ductile fracture in ferritic steels. The numerical parameters controlling the initial slope of the cohesive stress are set to $\alpha_{\mathsf{n}} = 2.3\ 10^4, \alpha_{\mathsf{t}} = \alpha_{\mathsf{s}} = 1.8\ 10^5$. Those values lead to an initial stiffness of the cohesive stress of the order of $10^{17}\, Pa/m$ in both normal and tangential directions. An estimate of those parameters as a function of the GTN material properties is given in appendix B in [1].

Two vertical displacement increments, U_y and $-U_y$, are simultaneously applied at the two upper and lower pin holes, respectively. Both pin holes are partially filled with a purely elastic material having the same elastic properties than the specimen

Table 1 Material parameters of the study.

Elasticity	$E\,(GPa)$	ν							
	205	0.3							
Hardening	$\sigma_0(MPa)$	K	n						
	376	900	7.2						
GTN	f_0	f_c	f_f	ε_N	s_N	f_N	q_1	q_2	
	0.001	0.05	0.2	0.3	0.05	0.2	1.25	1	

material. A tie constraint is used on the nodes at the interface between the load pin and the specimen. Computation is made using an explicit finite element solver with an implicit contact resolution within a dynamical formulation [35]. A time step $\delta t = 1.6\,10^{-8} s$ is used. Since all the involved constitutive laws are time-independent, a high velocity ($\dot{U}_y = 0.2\,m.s^{-1}$) is prescribed in order to run the simulation in a reasonable time. The mass density is set to 7.8 10^3 kg/m^3 as a standard value for most of steels. It is worth mentioning that this implicit-explicit coupled cohesive-volumetric computation was approximatively performed in 60 days with 10 GB of RAM memory and 40 cores.

Results

Fig. 3 shows the load (Force F_y) vs Crack Opening Displacement (COD approximated here by $2\,U_y$) curve obtained from the simulation. The simulation reproduces the drop of the load typically observed in C(T) tests. Furthermore, Fig. 4 and Fig. 5 illustrate the high level of heterogeneity of the local fields in terms of von Mises stress and accumulated plastic strain. Two specific surfaces of the specimen are shown, namely, the mid-thickness surface (at $z = 0$, symmetry plane) and the side-surface (at $z = 10$ *mm*, free-edge surface). It is seen that large plasticity develops in the crack-front vicinity promoting stable crack propagation. Note that the zone with high level of accumulated plastic strain in the crack front vicinity is different for the two surfaces. It appears to have a more rounded shape on the mid-section surface than on the side-surface. Note also that this plastic zone is larger at the free surface near the rear of the specimen in the case of the mid-section surface compared to the side-surface. Fig. 6 shows the deformed mesh of the specimen geometry model with the separation of its crack lips (crack mouth) and von Mises stress distribution in the uncracked ligament. Fig. 7 shows the shape of the crack front for some COD values. According to the plot, the crack-front, initially straight and uniform through the thickness, propagates faster in the specimen midsection than near the side-surfaces. For a given value of the crack opening displacement, the crack extension Δa has the highest value at the midsection and sharply decreases when going from the mid-section to the side-surfaces. This kind of crack profile exhibiting a tunneling effect through specimen thickness has been observed both numerically and experimen-

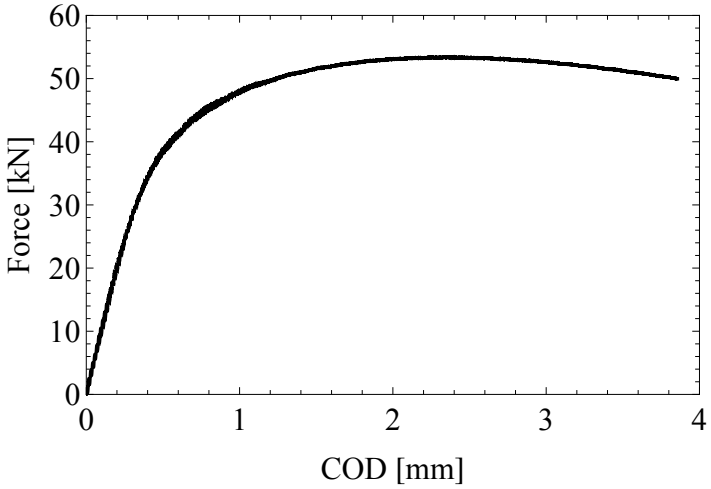

Fig. 3 Load (Force F_y) vs. Crack Opening Displacement (COD approximated by $2U_y$) curve obtained from the 3D numerical simulation of a compact tension fracture specimen.

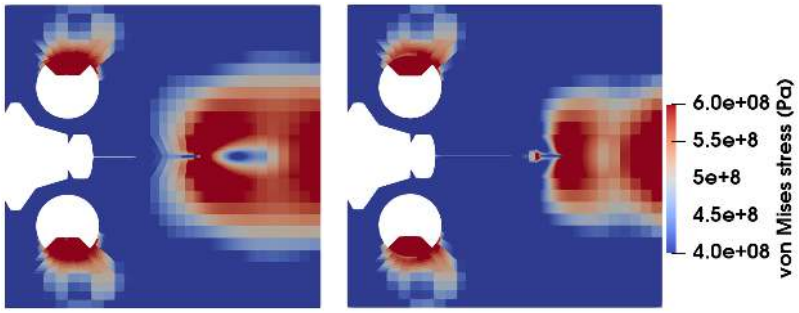

Fig. 4 Half-symmetric, 3D FE simulation of the C(T) specimen with smooth side-surfaces. Von Mises stress field on the smooth side-surface (left) and at the midsection-surface corresponding to the symmetry plane (right). Initial configuration. $U_y = 1.9244$ *mm*.

tally for specimen geometries with smooth side-surfaces [43, 44, 6, 45, 46]. From a microscopic point of view, the gradient of local constraint through the thickness leads to a damage mainly governed by void growth at the center of the specimen and shear dominated conditions at the side surface, the latter often leading to shear-lip formation [46]. Note that the crack growth due to shear dominated conditions at edges is limited in the current simulation since the cohesive model is based on the GTN model which predicts low damage at low triaxiality. Nevertheless, the simulation can still predict crack growth through the entire thickness of the specimen. Fig. 8 shows the evolution of the stress triaxiality during loading. It is plotted at the initial crack tip (at a_0) for different points through the thickness (different z values). This figure illustrates the strong heterogeneity of the stress triaxiality through the

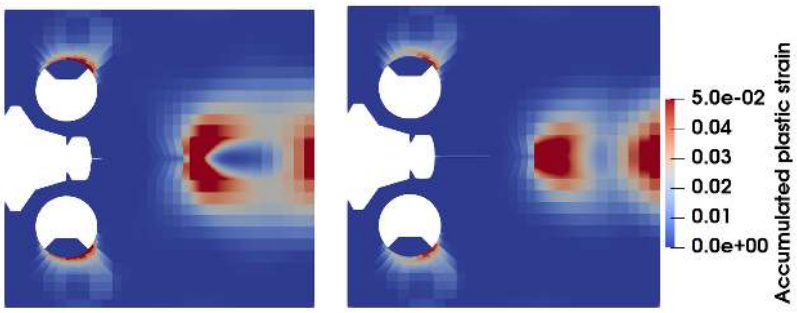

Fig. 5 Half-symmetric, 3D FE simulation of the C(T) specimen with smooth side-surfaces. Accumulated plastic strain field on the smooth side-surface (left) and at the midsection-surface (right). Initial configuration. Initial configuration. $U_y = 1.9244\ mm$.

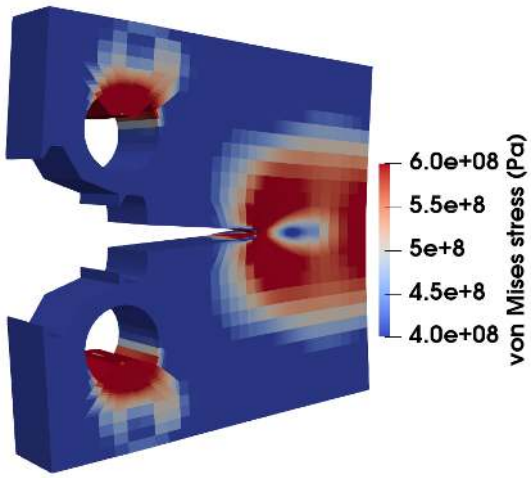

Fig. 6 Half-symmetric, 3D FE simulation of the C(T) specimen. Deformed mesh: opening of crack lips and von Mises stress localization during ductile crack propagation. $U_y = 1.9244\ mm$.

thickness and also its complex evolution during loading. It appears that the stress triaxiality is higher at the midsection ($z = 0$) than at the side-surface ($z = 10\ mm$). Fig. 9 shows the stress triaxiality with respect to the position through the thickness for different COD values. Here, it is plotted at the maximum current crack tip (at $a(t, z = 0)$). It appears that the stress triaxiality is relatively high at the midsection and sharply decreases at the side-surface. The observation that the crack advances faster in the midsection than at the side-surfaces is related to a higher stress triaxiality at midsection than at the side-surfaces. Let us recall that, in the cohesive model, damage is related to cavity growth. This cavity growth is controlled by the trace of the plastic strain rate. The high values of the stress triaxiality observed here should induce high values of the triaxiality of the strain rate in the cohesive model (the strain rate triaxiality in the cohesive model depends on the local stress around

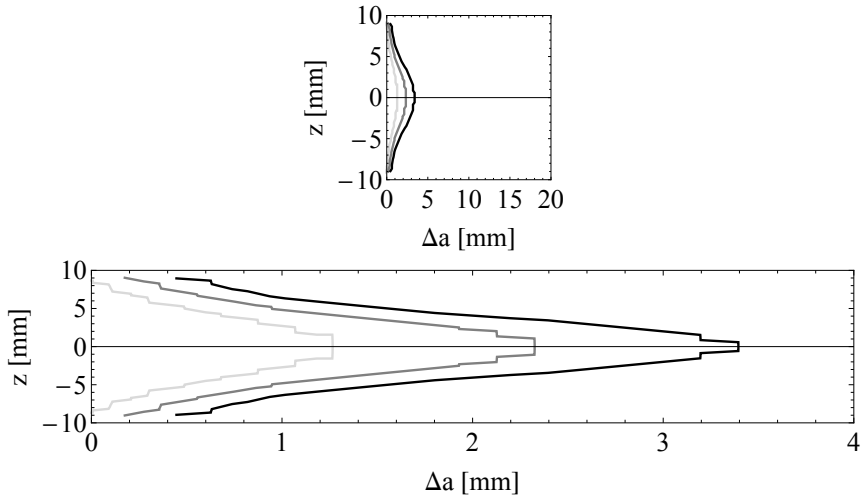

Fig. 7 Evolution of the crack front. COD $\simeq 1.67mm$, (light gray line), COD $\simeq 2.08$ *mm* (gray line), COD $\simeq 2.5$ *mm* (dark line). Top: crack in real dimensions. Bottom: figure is stretched in the crack extension direction for a better visualization. COD approximated by $2U_y$.

the cohesive zone through equation (15)), which should favor cavity growth and damage. This is verified in Fig. 10 which displays the strain triaxiality η_ε^{vol} at the crack front (remind that under the assumption of proportional loading, the strain rate triaxiality in the cohesive zone is equal to the strain triaxiality, see paragraph related to the implementation of the cohesive zone model into XPER). It is seen that the peak of the strain rate triaxiality is reached faster in the midsection than on the side-surface.

The spatial and temporal heterogeneity of the stress and strain triaxiality fields lead to various traction-separation responses along the crack-front as it is depicted in Fig. 11. From this figure, it can be observed that a higher peak cohesive stress is obtained at midsection (points with label "A") than at the side surface (points with label "D"). Moreover, at midsection, the peak cohesive stress increases between the positions "1" and "2" and then seems to stabilize between the positions "2" to "3". An opposite trend is obtained at the side surface where the peak cohesive stress decreases between the positions "1" and "2" and then seems to stabilize between the positions "2" and "3". As pointed out in [1], a significant feature of the cohesive model is that the shape of the local cohesive response is not a priori given but directly arises from the loading and the micromechanical model. In a close way, at midsection the shape of the cohesive response goes from a door-like model to a triangular model during crack propagation. At side surface, the overall shape does not vary significantly but the curve seems more flattened and spread out. From this figure, the surface cohesive energy (estimated as the area under the curve) is computed and reported in Fig. 12. The surface cohesive energy is higher at midsection than at the side surface. At midsection and side surface, it decreases between the positions

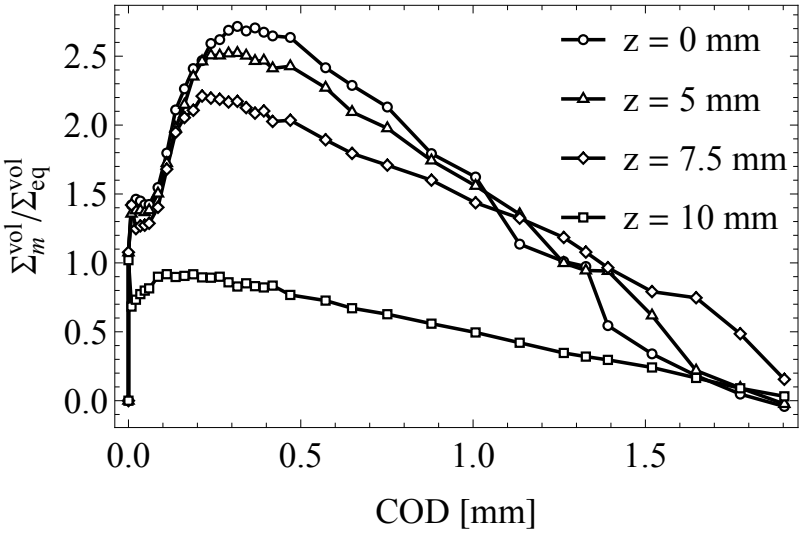

Fig. 8 Evolution of stress triaxiality with respect to Crack Opening Displacement (COD approximated by $2U_y$). Stress triaxiality is reported at the initial crack tip (at a_0) for four distinct points through the thickness (four distinct z values).

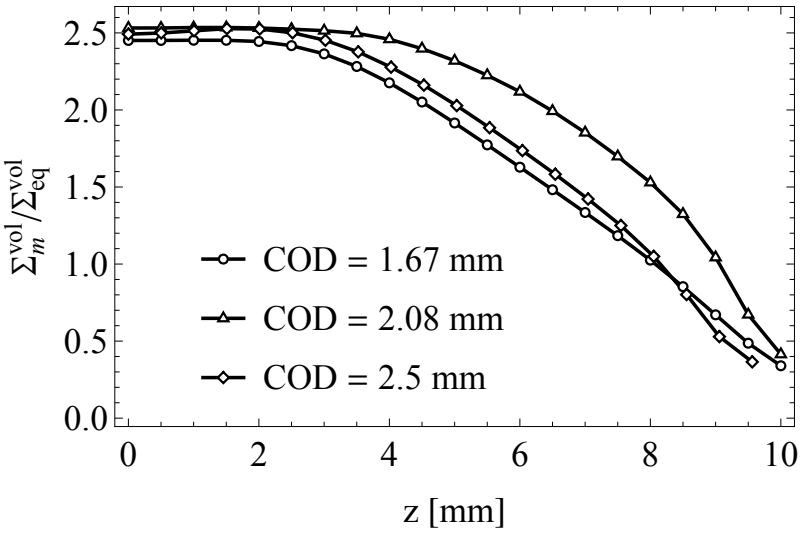

Fig. 9 Evolution of the stress triaxiality through the thickness for different COD values (approximated by $2U_y$). Stress triaxiality is reported at the maximum current crack tip (at $a(t, z = 0)$).

"1" and "2" and then seems to stabilize between the positions "2" and "3". At intermediate points (points with labels "B" and "C"), it increases between the positions "1" and "2" and then seems to stabilize between the positions "2" and "3". After a

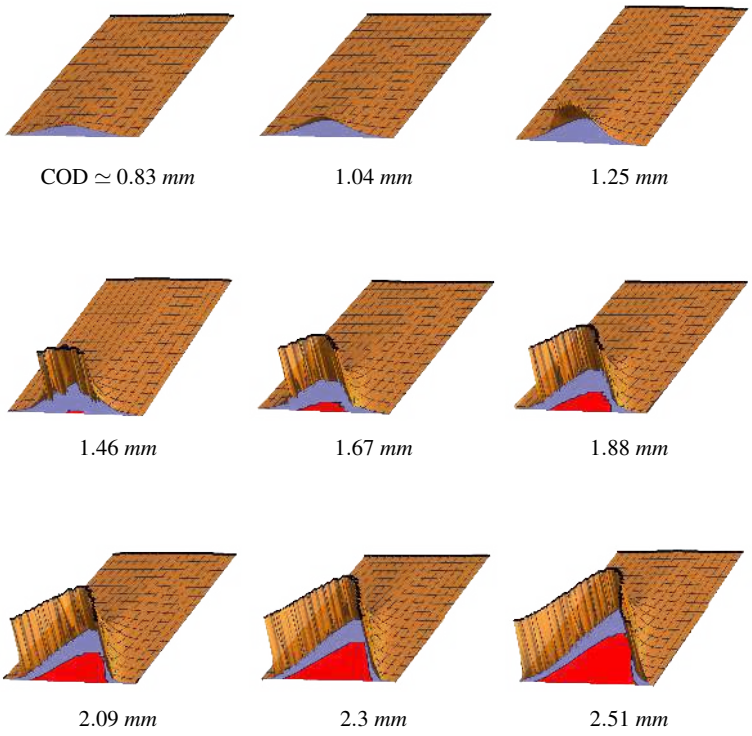

Fig. 10 Strain triaxiality field $\eta_{\varepsilon}^{\mathsf{vol}}$ (yellow) and crack surface (red) for different COD values (approximated by $2\,U_y$). The triaxiality field is clipped above the value of 0.2.

phase of crack propagation initiation, it appears that the crack propagation is done at a steady state.

Conclusion

This chapter presented a 3D numerical simulation of ductile crack growth in a 20 *mm* thick compact tension C(T) fracture specimen with smooth side-surfaces made of a ferritic steel by employing a cohesive model. This cohesive model was developed in [1] by incorporating the concepts of micromechanics based upon the GTN poroplasticity model within a cohesive zone model. The traction-separation law of the cohesive model derives from the projection of the volumetric GTN damage model onto a cohesive kinematics. It takes into account the effect of local I1 and J2 stress invariants via a dependence of the cohesive model to the surround-

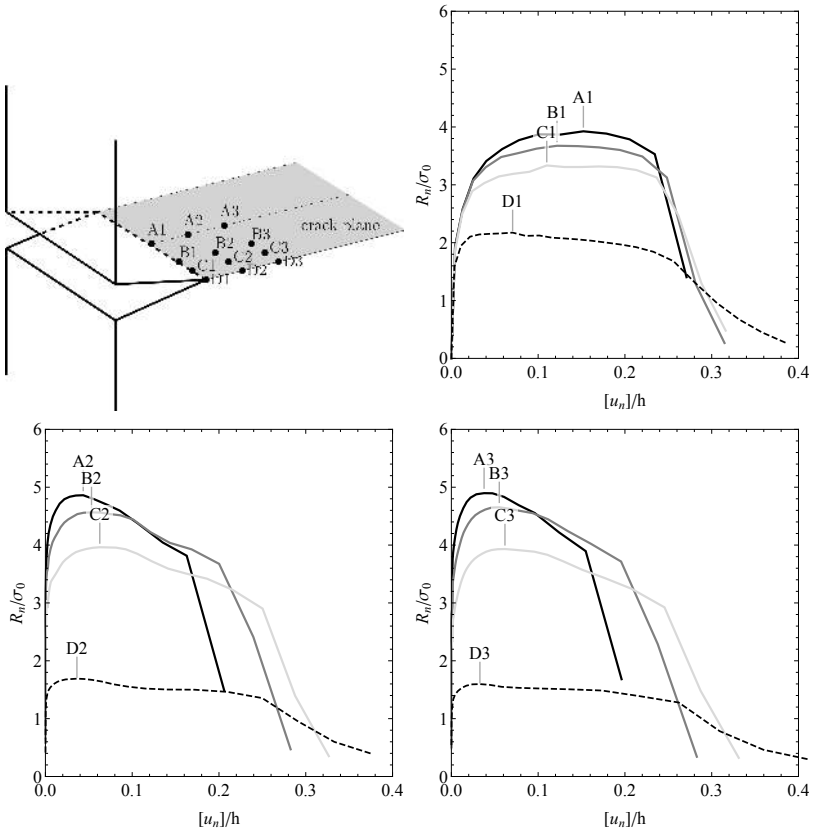

Fig. 11 Local cohesive responses at distinct points: normal cohesive stress with respect to normal displacement jump (normalized values).

ing bulk stress. The simulation showed a high level of heterogeneity of von Mises stress and accumulated plastic strain fields in the specimen. Moreover, the simulation showed that the crack growth profile through the thickness exhibits a relatively strong tunneling effect. During the simulation, it appears that the crack-front, initially straight and uniform through the thickness, propagates faster in the specimen midsection than near the side-surfaces. It is shown that this crack-front extension is related to a higher stress triaxiality at midsection than at the side-surfaces. It is also shown that the peak of the strain triaxiality is reached faster in the midsection than on the side-surfaces which favors damage by cavity growth. After a phase of crack propagation initiation, the local cohesive response stabilize leading to a steady state propagation of the crack. All the findings provided from the present simulation are consistent with the literature observations. Hence, this triaxiality dependent cohesive GTN model seems relevant to deal with problems of ductile fracture in thick-specimen made of ferritic steel but also in thick components. The model effi-

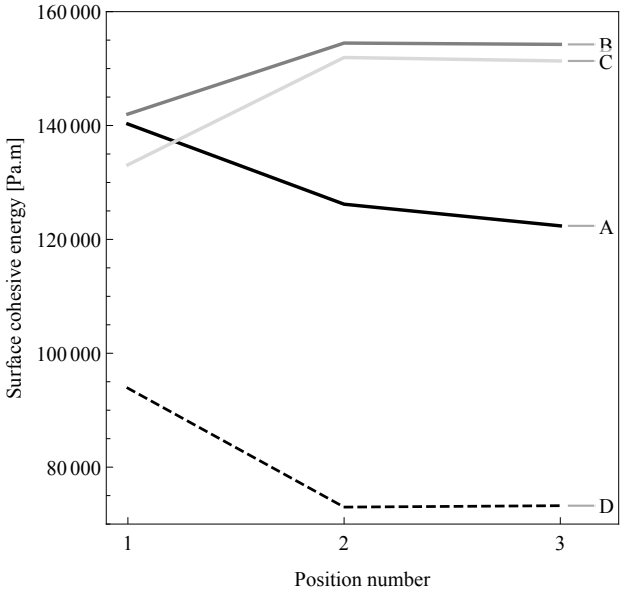

Fig. 12 Local surface cohesive energy at distinct points.

ciency could be tested in the case of crack initiation and propagation in other types of fracture specimens in order to estimate the feasibility of transfer of ductile tearing properties from specimens to components, which remains a challenging task. This is the scope of next coming works.

Acknownledgments

The project ATLAS+ (Advanced Structural Integrity Assessment Tools for Safe Long Term Operation) has received funding from the Euratom research and training programme 2014-2018 under the grant agreement No.: 754589. The project is jointly funded by the EU and individual partners. M. M. and F. P. thank the EU and all the ATLAS+ contributors for their support and contributions.

References

1. N.B. Nkoumbou Kaptchouang, Y. Monerie, F. Perales, P.G. Vincent, Engineering Fracture Mechanics **242**(107437) (2021)
2. Y.A. Roy, R.H. Dodds Jr., International Journal of Fracture **110**, 21 (2001)
3. S. Roychowdhury, Y.D. Arun Roy, R.H. Dodds, Engineering Fracture Mechanics **69**(8), 983 (2002). DOI 10.1016/S0013-7944(01)00113-8

4. I. Scheider, W. Brocks, Computational Materials Science **37**(1), 101 (2006). DOI 10.1016/j.commatsci.2005.12.042
5. I. Scheider, M. Schödel, W. Brocks, W. Schönfeld, Engineering Fracture Mechanics **73**(2), 252 (2006). DOI 10.1016/j.engfracmech.2005.04.005
6. C. Chen, O. Kolednik, J. Heerens, F. Fischer, Engineering Fracture Mechanics **72**, 2072 (2005)
7. I. Scheider, W. Brocks, Key Engineering Materials - KEY ENG MAT **251**, 313 (2003). DOI 10.4028/www.scientific.net/KEM.251-252.313
8. K.H. Schwalbe, I. Scheider, A. Cornec, Guidelines for Applying Cohesive Models to the Damage Behaviour of Engineering Materials and Structures (Springer Science & Business Media, 2012)
9. J.J.C. Remmers, R. de Borst, C.V. Verhoosel, A. Needleman, International Journal of Fracture **181**(2), 177 (2013). DOI 10.1007/s10704-013-9834-3
10. A.L. Gurson, Journal of Engineering Materials and Technology **99**(1), 2 (1977). DOI 10.1115/1.3443401
11. V. Tvergaard, International Journal of Fracture **17**(4), 389 (1981). DOI 10.1007/BF00036191
12. V. Tvergaard, A. Needleman, Acta Metallurgica **32**(1), 157 (1984). DOI 10.1016/0001-6160(84)90213-X
13. J. Koplik, A. Needleman, International Journal of Solids and Structures **24**(8), 835 (1988). DOI 10.1016/0020-7683(88)90051-0
14. V. Tvergaard, J.W. Hutchinson, Journal of the Mechanics and Physics of Solids **40**(6), 1377 (1992). DOI 10.1016/0022-5096(92)90020-3
15. V. Tvergaard, J.W. Hutchinson, International Journal of Solids and Structures **33**(20), 3297 (1996). DOI 10.1016/0020-7683(95)00261-8
16. V. Tvergaard, in IUTAM Symposium on Nonlinear Analysis of Fracture, Solid Mechanics and its Applications (Springer, Dordrecht, 1997), pp. 93–104
17. T. Siegmund, W. Brocks, International Journal of Fracture **99**(1-2), 97 (1999)
18. T. Siegmund, W. Brocks, (2000). DOI 10.1520/STP13400S
19. T. Siegmund, W. Brocks, Engineering Fracture Mechanics **67**(2), 139 (2000). DOI 10.1016/S0013-7944(00)00054-0
20. I. Scheider, Engineering Fracture Mechanics **76**(10), 1450 (2009). DOI 10.1016/j.engfracmech.2008.12.006
21. A. Banerjee, R. Manivasagam, Engineering Fracture Mechanics **76**(12), 1761 (2009). DOI 10.1016/j.engfracmech.2009.03.009
22. M. Anvari, I. Scheider, C. Thaulow, Engineering Fracture Mechanics **73**(15), 2210 (2006). DOI 10.1016/j.engfracmech.2006.03.016
23. M. Anvari, J. Liu, C. Thaulow, International Journal of Fracture **143**(4), 317 (2007). DOI 10.1007/s10704-007-9062-9
24. K.L. Nielsen, J.W. Hutchinson, International Journal of Impact Engineering **48**, 15 (2012)
25. P.B. Woelke, M.D. Shields, J.W. Hutchinson, Engineering Fracture Mechanics **147**, 293 (2015)
26. R.G. Andersen, P.B. Woelke, K.L. Nielsen, European Journal of Mechanics / A Solids **71**, 199 (2018)
27. R.G. Andersen, C.L. Felter, K.L. Nielsen, International Journal of Solids and Structures **160**, 265 (2019)
28. J.C. Michel, P. Suquet, F. Thébaud, Revue Européenne des Éléments Finis **3**(4), 573 (1994). DOI 10.1080/12506559.1994.10511149
29. J. Oliver, M. Cervera, O. Manzoli, International Journal of Plasticity **15**(3), 319 (1999). DOI 10.1016/S0749-6419(98)00073-4
30. M.G. Kulkarni, K. Matouš, P.H. Geubelle, International Journal for Numerical Methods in Engineering **84**(8), 916 (2010). DOI 10.1002/nme.2923
31. J. Oliver, International Journal of Solids and Structures **37**(48), 7207 (2000). DOI 10.1016/S0020-7683(00)00196-7
32. P.M. Suquet, in Nonsmooth Mechanics and Applications, International Centre for Mechanical Sciences (Springer, Vienna, 1988), pp. 279–340

33. C.C. Chu, A. Needleman, Journal of Engineering Materials and Technology **102**(3), 249 (1980)
34. F. Perales, S. Bourgeois, A. Chrysochoos, Y. Monerie, Engineering Fracture Mechanics **75**(11), 3378 (2008). Local Approach to Fracture (1986–2006): Selected papers from the 9th European Mechanics of Materials Conference
35. F. Perales, F. Dubois, Y. Monerie, B. Piar, L. Stainier, European Journal of Computational Mechanics **19**(4), 389 (2010)
36. M. Jean, V. Acary, Y. Monerie, Philosophical Transactions of the Royal Society A: Mathematical, Physical and Engineering Sciences **359**(1789), 2497 (2001)
37. V. Acary, Y. Monerie, Nonsmooth fracture dynamics using a cohesive zone approach. Research Report, INRIA (2006)
38. S. Cravero, C. Ruggieri, Engineering Fracture Mechanics **72**(1), 1344 (2005)
39. W. Brocks, A. Cornec, I. Scheider, Computational Aspects of Nonlinear Fracture Mechanics. Tech. rep., Institute of Materials Research GKSS research centre Geesthacht (2002). Technical Note GKSS/WMS/02/05
40. W. Brocks, D. Steglich, Hybrid methods, chapter 11-07. doc, Comprehensive Structural Integrity – 11 mechanical characterization of materials. Tech. rep., GKSS Research Center (2006). Technical Note GKSS/WMS/02/05
41. L.A. Silva, S. Cravero, C. Ruggieri, Engineering Fracture Mechanics **73**, 2123 (2006)
42. X. Zhu, International Journal of Pressure Vessels and Piping **156**, 40 (2017)
43. X. Gao, J. Faleskog, C. Shih, Int. J. Fracture **89**, 375 (1998)
44. C. Chen, O. Kolednik, I. Siegmund, A. Tatschl, F. Fischer, International Journal of Fracture **120**, 517–536 (2003)
45. C. Chen, O. Kolednik, International Journal of Fracture **132**, 135 (2005)
46. M. Paredes, T. Wierzbicki, P. Zelenak, Engineering Fracture Mechanics **168**, 92–111 (2016)